

Quantum correlations of light from a room temperature mechanical oscillator for force metrology

V. Sudhir,^{1,*} R. Schilling,^{1,*} S. A. Fedorov,^{1,*} H. Schütz,^{1,*} D. J. Wilson,¹ and T.J. Kippenberg^{1,†}

¹*Institute of Physics (IPHYs), École Polytechnique Fédérale de Lausanne, Lausanne 1015, Switzerland*

(Dated: December 21, 2016)

The coupling of laser light to a mechanical oscillator via radiation pressure leads to the emergence of quantum mechanical correlations between the amplitude and phase quadrature of the laser beam. These correlations form a generic non-classical resource which can be employed for quantum-enhanced force metrology, and give rise to ponderomotive squeezing in the limit of strong correlations. To date, this resource has only been observed in a handful of cryogenic cavity optomechanical experiments. Here, we demonstrate the ability to efficiently resolve optomechanical quantum correlations imprinted on an optical laser field interacting with a room temperature nanomechanical oscillator. Direct measurement of the optical field in a detuned homodyne detector (“variational measurement”) at frequencies far from the resonance frequency of the oscillator reveal quantum correlations at the few percent level. We demonstrate how the absolute visibility of these correlations can be used for a quantum-enhanced estimation of the quantum back-action force acting on the oscillator, and provides for an enhancement in the relative signal-to-noise ratio for the estimation of an off-resonant external force, even at room temperature.

The radiation pressure interaction of light with mechanical test masses has been the subject of early theoretical research in the gravitational wave community [1, 2], leading for example, to an understanding of the quantum limits of interferometric position measurements. For a mechanical oscillator parametrically coupled to an optical cavity, the trade-off between radiation pressure quantum fluctuations of the meter beam (i.e. measurement back-action) and detected shot noise establishes a minimum uncertainty in the detection of the test mass (i.e. mirror) position, commonly referred to as the standard quantum limit [3, 4]. However the two noise contributions – measurement back-action and imprecision – are in general correlated. From the perspective of the transmitted light, the interaction with the mechanical oscillator causes quantum correlations among its degrees of freedom via the same radiation pressure quantum fluctuations. The fluctuations in the amplitude quadrature drive the mechanical oscillator, and this back-action driven motion is transduced into the phase quadrature. Correlations thus established form a valuable quantum mechanical resource: the optomechanical system may be viewed as an effective Kerr medium emitting squeezed states of the optical field [5, 6], or the correlations can be directly employed for back-action cancellation in the measurement record via “variational measurements” [7–9].

In practice, the difficulty in observing, and ultimately utilizing, these optomechanical quantum correlations is compounded by the presence of thermal noise. For a high quality-factor (Q) mechanical oscillator, its intrinsic thermal Brownian motion poses the largest source of contamination. In the past decade, the emergence of cavity opto- and electro-mechanical systems [10], incorporating high- Q mechanical oscillators operated at cryogenic temperatures, have enabled experiments in the quantum coherent regime where the optical field is the dominant bath seen by the mechanical oscillator. In particular, cryogenic experiments have accessed the regime

where mechanical motion driven by quantum fluctuations in the optical field is comparable to the thermal noise [11–13], enabling the study of various manifestations of optomechanically generated quantum correlations. In a heterodyne measurement, these correlations can give rise to an asymmetry of the mechanical sidebands generated by the optomechanical interaction [14–19], while in a homodyne measurement they lead to optical squeezing [11, 19–22]. Despite these advances, directly observing such quantum correlations at room temperature has remained elusive.

Here we describe an experiment that observes optomechanically generated quantum correlations at room temperature (ca. 300 K), and a proof-of-principle demonstration of their use in enhancing the ability to estimate forces. Homodyne detection of the transmitted meter field near the amplitude quadrature (“variational measurement” [7]), together with the ability to probe far away from the mechanical resonance frequency, allows us to detect signatures of the correlations established by a mechanical oscillator, circumventing the large $n_{\text{th}} \approx k_B T / \hbar \Omega_m \approx 10^6$ thermal phonon occupation. A complementary strategy, employing cross-correlation near mechanical resonance [23], has also recently succeeded in observing similar correlations up to room temperature [24]. In contrast to this contemporary experiment, we work in the regime where quantum back-action, quantified as an average phonon occupation n_{QBA} , forms an appreciable contribution to the oscillator’s motion, i.e. $n_{\text{QBA}} \gg 1$. Despite the fact that it is small compared to the thermal occupation n_{th} , i.e. $n_{\text{QBA}} \ll n_{\text{th}}$, we show that signature of quantum correlations in a variational measurement of the meter beam scales as $\sqrt{n_{\text{QBA}}/n_{\text{th}}}$, thus yielding a square-root enhancement in the ability to estimate the back-action force compared to conventional detection on phase quadrature [11–13]. Finally, we show how the signal-to-noise ratio for the estimation of an external force applied on the mechanical oscillator is improved by the presence of the same correlations. These experiments herald cavity optomechanics as a platform for room temperature quantum optics and quantum metrology.

Our system consists of a Si_3N_4 nanomechanical oscillator coupled dispersively to a whispering gallery mode of a sil-

* These authors contributed equally to this work

† tobias.kippenberg@epfl.ch

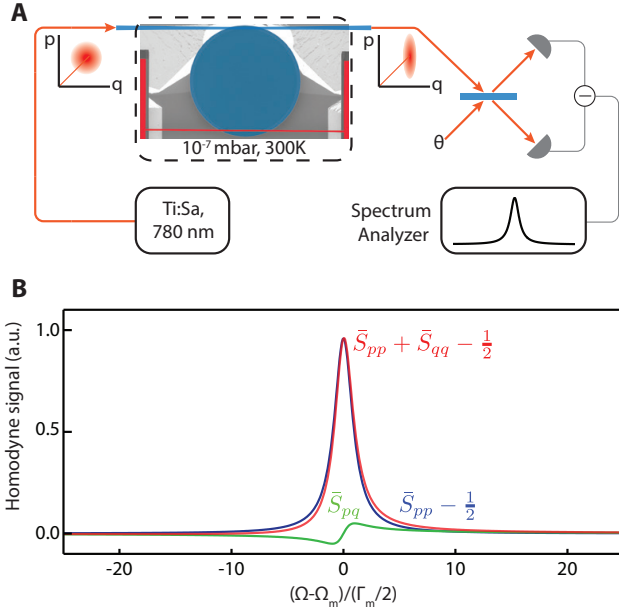


FIG. 1. Quantum correlations due to a room temperature optomechanical system. (A) Schematic of the experiment. Light from a Ti:Sa laser operating at 780 nm resonantly probes an optomechanical system maintained at room temperature ($T \approx 300$ K) in a low pressure ($\approx 10^{-7}$ mbar) vacuum chamber. The transmitted laser light is analysed in a balanced homodyne detector whose local oscillator phase θ is variable. The input light, in a coherent state as represented by the phase space cartoon, is transformed into one containing correlations between its amplitude and phase fluctuations, after interacting with the optomechanical system. Tuning θ gives access to different meter beam quadratures $\delta q_\theta(t)$. (B) Illustration of the homodyne photocurrent spectrum $\bar{S}_{II}^{\theta \approx 0}[\Omega]$ (red trace) showing asymmetry due to quantum correlations in the transmitted optical beam. The signal (red) may be understood to arise from a symmetric contribution (blue) consisting of the total motion of the oscillator (consisting of the thermal and back-action contributions), and an asymmetric contribution (green) due to quantum correlations, as shown in eqs. (2) and (3).

ica disk cavity [25]. By placing the beam in close proximity (≈ 50 nm) to the disk, together with an increased participation ratio of the oscillator (see SI), a vacuum optomechanical coupling rate of $g_0 \approx 2\pi \cdot 60$ kHz is attained – a factor of three

increase compared to recent cryogenic experiments [12, 19]. Together with the high mechanical $Q \approx 3 \cdot 10^5$ (corresponding to a decay rate of $\Gamma_m \approx 2\pi \cdot 12$ Hz) and an optical cavity in the bad-cavity limit (cavity decay rate, $\kappa \approx 2\pi \cdot 4.5$ GHz, mechanical resonance frequency $\Omega_m \approx 2\pi \cdot 3.4$ MHz) the device attains a near unity single photon cooperativity, $C_0 = 4g_0^2/\kappa\Gamma_m \approx 0.27$, at room temperature. Specific aspects of the device fabrication and general room temperature performance are detailed elsewhere [25].

In the experiment (see fig. 1A), the optomechanical device is placed in a high-vacuum chamber and probed on resonance using a Ti:Sa laser. The transmitted phase quadrature fluctuations, $\delta p_{\text{out}} = -\delta p_{\text{in}} + \sqrt{2C\Gamma_m}(\delta x/x_{\text{zp}})$, in the frame rotating with the meter laser (see SI), carries information regarding the total motion δx of the mechanical oscillator; here $C = C_0 n_c$ is the multi-photon cooperativity, n_c is the mean intracavity photon number, and $x_{\text{zp}} = \sqrt{\hbar/2m\Omega_m}$ is the zero-point motion of the oscillator. The total motion $\delta x = \delta x_{\text{th}} + \delta x_{\text{QBA}}$, contains a component due to the thermal Brownian motion of the oscillator, $\delta x_{\text{th}}[\Omega] = \chi[\Omega]\delta F_{\text{th}}[\Omega]$, and a quantum back-action driven motion, $\delta x_{\text{QBA}}[\Omega] = \chi[\Omega]\delta F_{\text{QBA}}[\Omega] = \sqrt{2C\Gamma_m}(\hbar\chi[\Omega]/x_{\text{zp}})\delta q_{\text{in}}[\Omega]$, that is due to the quantum fluctuations in the amplitude of the meter field. Here $\chi[\Omega] = m^{-1}(\Omega_m^2 - \Omega^2 - i\Omega\Gamma_m)^{-1}$ is the susceptibility of the mechanical oscillator's position to an applied force at frequency Ω . Importantly, the optomechanical interaction establishes quantum correlations between the light's amplitude and phase; the symmetrized cross-correlation spectrum [4], $\bar{S}_{pq}^{\text{out}}[\Omega] = \int \langle \frac{1}{2} \{ \delta p_{\text{out}}(t), \delta q_{\text{out}}(0) \} \rangle e^{i\Omega t} dt$ characterizes the magnitude of these correlations. Explicitly (see SI),

$$\bar{S}_{pq}^{\text{out}}[\Omega] = C\Gamma_m \text{Re} \frac{\hbar\chi[\Omega]}{x_{\text{zp}}^2}, \quad (1)$$

i.e. a large correlation between the transmitted phase and amplitude, proportional to the multi-photon cooperativity C , is established around the mechanical frequency.

These correlations can be directly observed by measuring the transmitted optical field in a homodyne detector with a local oscillator phase θ , corresponding to a measurement of the rotated quadrature, $\delta q_{\text{out}}^\theta = \delta q_{\text{out}} \cos \theta + \delta p_{\text{out}} \sin \theta$. In this case, the homodyne photocurrent spectrum (referred to electronic shot noise) takes the form (see SI),

$$\begin{aligned} \bar{S}_{II}^\theta[\Omega] &= \cos^2 \theta \bar{S}_{qq}^{\text{out}}[\Omega] + \sin^2 \theta \bar{S}_{pp}^{\text{out}}[\Omega] + \sin(2\theta) \bar{S}_{pq}^{\text{out}}[\Omega] \\ &\propto 1 + \frac{4\eta C\Gamma_m}{x_{\text{zp}}^2} \left(\sin^2 \theta |\chi[\Omega]|^2 (\bar{S}_{FF}^{\text{th}}[\Omega] + \bar{S}_{FF}^{\text{QBA}}[\Omega]) + \sin(2\theta) \frac{\hbar}{2} \text{Re} \chi[\Omega] \right), \end{aligned} \quad (2)$$

where η is the detection efficiency. The quantum correlations in the output field (third term in eq. (2)) can be observed despite the large thermal noise (second term in eq. (2)) by exploiting, firstly, the difference in the dependence of the cor-

relation term on the local oscillator phase, and secondly, its dependence on the mechanical susceptibility. Specifically, by operating close to the amplitude quadrature ($\theta = 0$) and at Fourier frequency detuning, $\delta \equiv \Omega - \Omega_m$, far from mechani-

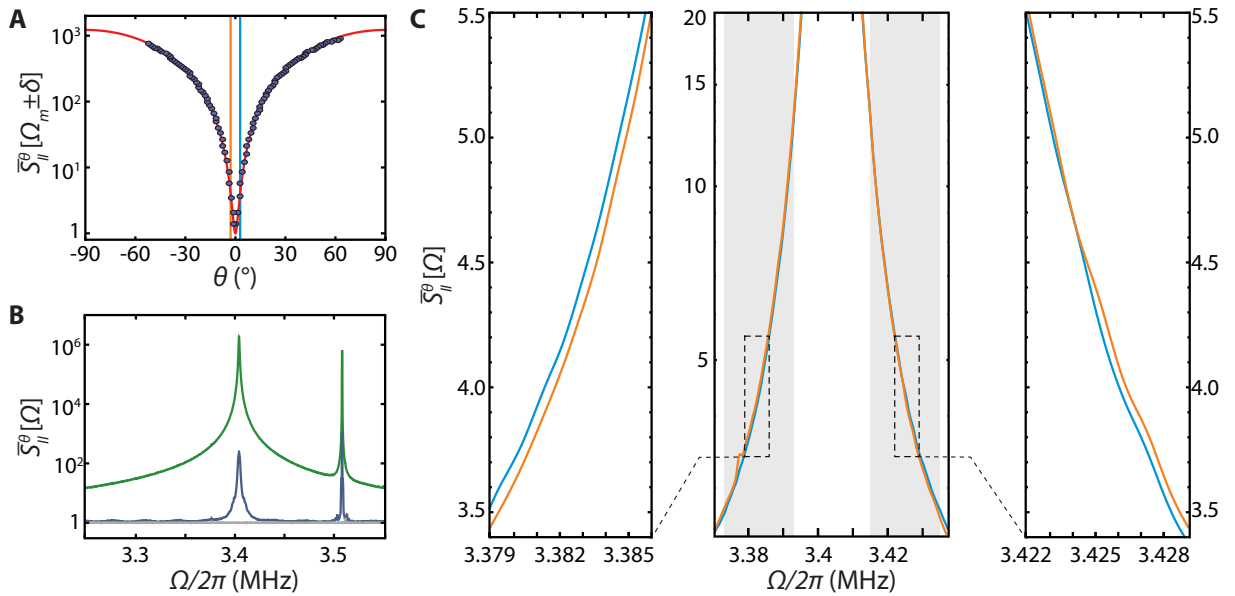


FIG. 2. **Asymmetry in homodyne spectrum.** (A) Measured variation of the photocurrent signal-to-noise, $\bar{S}_{II}^{\theta}[\Omega_m]$ (normalized to shot-noise), as the homodyne angle, θ , is varied. A 32 dB suppression of the resonant signal, proportional to the total motion, is achieved in the amplitude quadrature, limited by residual fluctuations in the homodyne angle ($\theta_{\text{RMS}} < 0.01$ rad). (B) Examples of spectra taken near the phase (green) and amplitude (blue) quadratures, together with the shot-noise background (gray) estimated by blocking the meter laser path in the homodyne detector. For all measurements, feedback is used to stabilize the mode, as discussed in the text. (C) Zoom-in of the spectrum at two quadratures, $\pm\theta$, approximately symmetric about the amplitude quadrature, shown as blue ($+\theta$) and yellow ($-\theta$) cuts in (A). Quantum correlations manifest as a slight asymmetry between the two spectra, leading to $\bar{S}_{II}^{+\theta}[\delta < 0] > \bar{S}_{II}^{-\theta}[\delta < 0]$ and visa versa for frequencies $\delta > 0$. Larger asymmetry is observed for frequency offsets further from mechanical resonance, i.e. $|\delta| \gg \Gamma_m$, as predicted by eq. (3). The data shown here corresponds to a resolution bandwidth of 1 kHz, much smaller than the frequency bands over which the asymmetry is observed. The shaded gray regions show cuts used for all data sets to systematically analyse the asymmetry as the homodyne angle is varied; see text for details.

cal resonance ($|\delta| \gtrsim \Gamma_m$), the contribution of the total thermal noise, $n_{\text{tot}} = n_{\text{th}} + n_{\text{QBA}}$, can be suppressed relative to the correlation contribution. Here $n_{\text{QBA}} = C$ is the phonon occupation due to measurement back-action. These constraints imply $n_{\text{QBA}} \gtrsim n_{\text{th}}$ for quantum correlations to dominate the homodyne signal.

The large thermal occupation of room temperature mechanical oscillators makes it technically challenging to achieve $n_{\text{QBA}} > n_{\text{th}}$, required for example for the observation of room temperature ponderomotive squeezing. However, even in the regime where $n_{\text{QBA}} < n_{\text{th}}$, the presence of quantum correlations can be witnessed for frequency offsets sufficiently large compared to the damping rate, while still small compared to the decoherence rate, i.e. $n_{\text{th}}\Gamma_m \gtrsim |\delta| \gg \Gamma_m$. In this regime, the effect of quantum correlation is to cause an asymmetry in the homodyne photocurrent spectrum,

$$\bar{S}_{II}^{\theta}[\delta]_{|\delta| \gg \Gamma_m} \approx 1 + 4\eta C n_{\text{tot}} \left(\frac{\Gamma_m}{\delta} \sin \theta \right)^2 - 2\eta C \left(\frac{\Gamma_m}{\delta} \sin 2\theta \right), \quad (3)$$

between positive ($\delta > 0$) and negative ($\delta < 0$) offsets from the mechanical frequency [23, 26]. Note that such an asymmetric response can also arise from quantum correlations present a priori in the meter beam, as for example in a recent demon-

stration in an electromechanical system employing a squeezed meter field [27]. Figure 1B shows a schematic of an asymmetric spectrum of the homodyne photocurrent for a representative quadrature close to the amplitude, i.e. $\theta \approx 0$; red shows the asymmetric spectrum that should be observed at sufficient measurement strength, while blue and green traces show the contributions due to thermal motion and quantum correlations respectively. Note that unlike ponderomotive squeezing, the ability to discern such weak correlations does not hinge on being able to realize $Q \gtrsim n_{\text{th}}$.

As shown in fig. 1A, this measurement strategy is applied to the fundamental out-of-plane mode of a Si_3N_4 nanostring at room temperature ($T = 300$ K) measured using a Ti:Sa laser at 780 nm. In order to mitigate optomechanical instabilities, an auxiliary laser at 850 nm, locked to the wing of an independent cavity mode is used to feedback-cool the fundamental mode (see SI for experimental schematic). Feedback damps the oscillator to an effective linewidth of $2\pi \cdot 1$ kHz; however, its decoherence rate, $n_{\text{th}}\Gamma_m$, and thus the quantum cooperativity [10], C/n_{th} , remains unchanged. Therefore, from the perspective of the meter laser, feedback does not alter the ratio of quantum correlations to thermal noise. Figure 2A shows the sensitivity of the homodyne interferometer as a function of the local oscillator phase θ . By operating with a modest input power of $25 \mu\text{W}$, we measure thermal motion of the oscillator with an imprecision, $n_{\text{imp}} = (16\eta C)^{-1} \approx 1.2 \cdot 10^{-4}$,

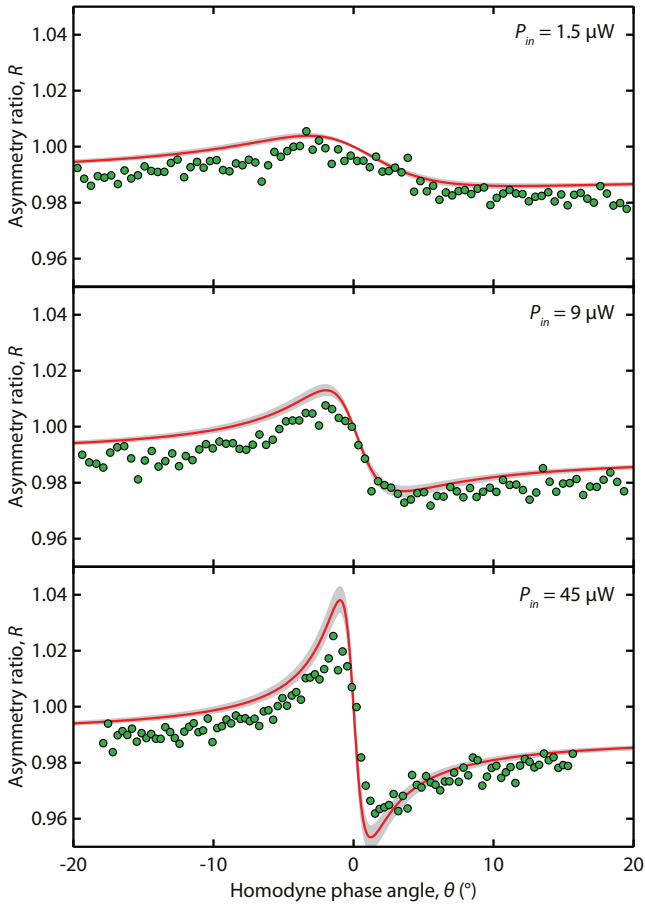


FIG. 3. **Asymmetry in homodyne spectrum as a function of quadrature angle.** Each plot shows asymmetry of the homodyne spectra, R_θ (eq. (4)), as a function of homodyne angle. From top to bottom, R_θ is plotted as the probe power (mean intracavity photon number) is increased, $P_{in} = 1.5, 9, 45 \mu W$ ($n_c \approx 0.3 \cdot 10^4, 2.1 \cdot 10^4, 10 \cdot 10^4$). Red lines show predictions from a model employing only quantum noises and independently inferred values of the input power P_{in} , and effective single-photon cooperativity, ηC_0 ; gray shows intervals corresponding to statistical uncertainties in either parameter.

that is approximately 40 dB below that at the standard quantum limit (corresponding to $n_{imp} = 1/4$) while operating on phase quadrature ($\theta = \pi/2$). As the local oscillator phase is swept towards the amplitude quadrature ($|\theta| \rightarrow 0$), thermal motion is effectively suppressed. Figure 2B shows example photocurrent spectra measured close to the phase (green) and amplitude (blue) quadratures; the gray trace shows shot-noise of the homodyne detector, recorded by blocking the meter field. Despite the meter laser being intrinsically quantum-noise-limited in the amplitude quadrature (see SI), we notice noise in the transmitted amplitude quadrature $\approx 20\%$ in excess of shot-noise, at this operating power. As shown in detail in the SI, this noise originates from thermomechanical motion of higher order vibrational modes of the tapered fiber that are transduced to amplitude and phase fluctuations by the cavity.

In order to discern any asymmetry in the photocurrent spec-

tra as predicted by eq. (3), we choose two spectra symmetric about the amplitude quadrature, indicated by the blue (at phase $+\theta$) and yellow (at phase $-\theta$) vertical lines in fig. 2A; the corresponding spectra are shown in fig. 2C. The central panel of fig. 2C shows a portion of the two spectra for frequency offsets far from resonance, i.e. $|\delta| < 3 \cdot 10^3 \cdot \Gamma_m$. Insets to the left and to the right show portions of the photocurrent spectra symmetric about resonance, and at an offset $|\delta| \approx 2 \cdot 10^3 \cdot \Gamma_m$. An asymmetry between the spectra at the level of $\approx 5\%$ is observed, consistent with the theoretically predicted effect due to quantum correlations.

Next, we systematically investigate this asymmetry. The asymmetry in the observed spectrum (red in fig. 1B) traces its root to the asymmetric contribution of the quantum correlations (green in fig. 1B, and third term in eq. (3)). This asymmetry can be characterized by the ratio, $R_\theta \equiv \bar{S}_{II}^\theta[+\delta]/\bar{S}_{II}^\theta[-\delta]$, which is explicitly given by (see SI),

$$R_\theta = \frac{1 + 4\eta C n_{tot} (\Gamma_m \sin \theta / \delta)^2 (1 - (\delta / n_{tot} \Gamma_m) \cot \theta)}{1 + 4\eta C n_{tot} (\Gamma_m \sin \theta / \delta)^2 (1 + (\delta / n_{tot} \Gamma_m) \cot \theta)}. \quad (4)$$

Note that quantum correlations render R_θ anti-symmetric with respect to the local oscillator phase tuned through the amplitude quadrature ($\theta = 0$), i.e. $R_\theta - 1 \approx -(R_{-\theta} - 1)$, thus providing a robust experimental signature for the presence of such correlations, when noise in the amplitude and phase quadrature of the meter laser is sufficiently small (see SI and [19]). The ratio R_θ (defined in eq. (4)) is measured by recording the spectral power in windows of finite bandwidth symmetric about resonance (indicated as gray vertical bands in fig. 2C), as a function of the homodyne angle θ . Figure 3 shows R_θ as function of homodyne angle for several probe powers. At low probe powers (i.e. low cooperativity, $C \approx 8 \cdot 10^2$), shown in the top panel of fig. 3, the anti-symmetric feature around the amplitude quadrature (i.e. $R_\theta - 1$) is diminished by the low measurement im-

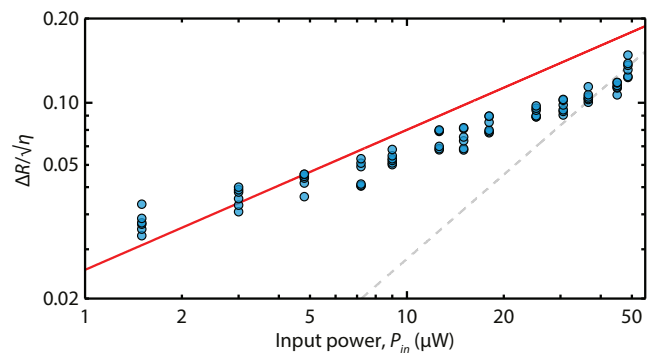


FIG. 4. **Visibility of quantum correlations versus laser power.** Plot shows the deviation of the ratio R_θ from its classical value of unity, i.e. ΔR , as a function of laser power. At each power, the blue points show the size of the dispersive feature in R_θ near $\theta = 0$, for various values of the detuning δ . The red line is a no-fit-parameter theoretical model including only quantum-noise-induced correlations, which predicts a square-root dependence on power. Gray dashed line shows a linear fit to the data.

cision. As the probe power is increased, shown in the two subsequent panels of fig. 3, the relative contribution of quantum correlation increases, leading to a progressively larger anti-symmetry near amplitude quadrature. The observed anti-symmetric feature around the amplitude quadrature is a characteristic of amplitude-phase correlations in the meter field. Classical sources of such anti-symmetric contributions, for example from laser phase noise, are negligible in our experiments, as are other sources of systematics (see SI for details).

For the scenario in our experiments, where the back-action occupation is appreciable, yet not larger than the thermal motion, i.e. $n_{\text{th}} \gg n_{\text{QBA}} \gg 1$, the maximum deviation of the asymmetry ratio R_θ , can be shown to take the form,

$$\Delta R \equiv \max_{\theta} R_\theta - \min_{\theta} R_\theta \approx 4 \sqrt{\eta \frac{n_{\text{QBA}}}{n_{\text{th}}}}. \quad (5)$$

On the one hand, this relation implies that despite $n_{\text{QBA}}/n_{\text{th}} \approx 10^{-3}$, it is eminently possible to estimate the back-action occupation via the square-root enhancement provided by the quantum correlations in the measurement record. On the other hand, this relation implies that a square-root scaling of ΔR with laser power is an unambiguous signature of the quantum mechanical origin of the correlations that lead to the spectral asymmetry. Figure 4 depicts the scaling of ΔR with probe power. Importantly, the agreement with a square-root scaling suggests that a dominant portion of the asymmetry witnessed in our experiments arises due to quantum correlations in the probe beam. Note that classical sources of noise would lead to a linear scaling of ΔR with meter laser power. For all data reported in fig. 4, ΔR is extracted by observing the asymmetry in the same spectral window around $|\delta| \approx 2 \cdot 10^3 \cdot \Gamma_m$ (shown as gray regions in fig. 2C).

These results signal the emergence of cavity quantum optomechanics at room temperature, and the possibility of room temperature quantum-enhanced metrology using such a platform. Quantum correlations form a generic resource for enhancing the precision with which parameters of a system can be estimated [28]. In our case, the ability to estimate a force δF_{ext} applied on a mechanical oscillator is hindered by fundamental sources of force-equivalent noise. It can be shown (see SI) that the spectral density of the unbiased force estimator $\delta F_{\text{est}}^\theta$, based on the observed homodyne photocurrent δI^θ , takes the form (see SI),

$$\bar{S}_{FF}^{\text{est},\theta}[\Omega] = \bar{S}_{FF}^{\text{ext}}[\Omega] + \bar{S}_{FF}^{\text{tot}}[\Omega] + \bar{S}_{FF}^{\text{imp},\theta}[\Omega] + \hbar \cot \theta \frac{\text{Re } \chi[\Omega]}{|\chi[\Omega]|^2}. \quad (6)$$

The uncertainty in the estimate of the applied force, $\bar{S}_{FF}^{\text{ext}}$, is due to a contribution from thermal motion and measurement back-action (second term, $\bar{S}_{FF}^{\text{tot}} = \bar{S}_{FF}^{\text{th}} + \bar{S}_{FF}^{\text{QBA}}$), a contribution due to measurement imprecision due to shot-noise in homodyne detection (third term), and a contribution due to quantum correlations (last term). By detecting away from the phase quadrature (i.e. $\theta \neq \pi/2$), non-zero correlations, potentially negative in magnitude, can be used to reduce the uncertainty in force estimation. In fact, in the limit where $\bar{S}_{FF}^{\text{QBA}} \gg \bar{S}_{FF}^{\text{imp},\pi/2}$ (practically, $C \gg 1$), and at an optimal measurement quadrature at angle θ_{opt} , the force estimator

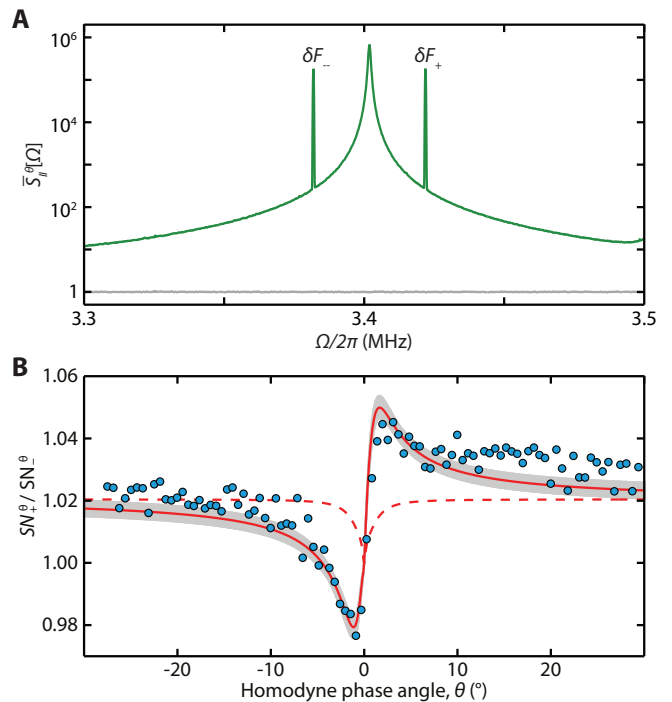


FIG. 5. **Quantum-enhanced external force estimation.** (A) Homodyne photocurrent spectrum near phase quadrature showing the two balanced forces applied on the mechanical oscillator via radiation pressure from the auxiliary laser. Here the meter laser power is $P_{\text{in}} = 30 \mu\text{W}$. (B) Relative signal-to-noise ratio (green), defined in eq. (8), as a function of the homodyne angle. For a force balanced in intensity and frequency offset from resonance, eq. (8) predicts a variation exactly the same as the variation of the asymmetry due to quantum correlations, R_θ . Red shows the prediction from theory, using known parameters of the experiment. Red dashed shows prediction from a theory excluding the contribution from quantum correlations.

spectrum is given by (see SI),

$$\bar{S}_{FF}^{\text{est},\theta_{\text{opt}}}[\Omega] = \bar{S}_{FF}^{\text{ext}}[\Omega] + \bar{S}_{FF}^{\text{th}}[\Omega] + \bar{S}_{FF}^{\text{imp},\pi/2}[\Omega] + \left[1 - \eta \left(\frac{\text{Re } \chi[\Omega]}{|\chi[\Omega]|} \right)^2 \right] \bar{S}_{FF}^{\text{QBA}}[\Omega]; \quad (7)$$

i.e., complete cancellation of measurement back-action is possible in the estimator at frequencies away from mechanical resonance, limited by the efficiency with which the noise that originally caused the back-action is detected (see SI). Note that in this scheme, back-action is cancelled only in the measurement record – different from back-action evasion [29]. In our experiment, since thermal motion is still the dominant contribution to the uncertainty in the force estimator, back-action cancellation by variational measurement gives only a meagre 0.01% improvement compared to the standard quantum limit for conventional detection. A contemporary cryogenic experiment projects a metrological gain of a few percent [30].

Despite the large thermal occupation, we are able to demonstrate the underlying concept of quantum-enhanced force metrology. To this end, we perform an experiment that shows

an improvement in the relative signal-to-noise ratio for the estimation of a coherent force. We consider an external force, $\delta F_{\text{ext}}[\Omega] = \delta F_+ \delta[\Omega_F + \delta] + \delta F_- \delta[\Omega_F - \delta]$, consisting of two coherent components δF_{\pm} at frequencies symmetric about Ω_F . For the variational measurement strategy, the signal-to-noise ratio, SN_{\pm}^{θ} , for the detection of either component, benefits from the presence of quantum correlations in the meter beam. In fact, the relative signal-to-noise ratio of the two components (see SI),

$$\frac{\text{SN}_+^{\theta}}{\text{SN}_-^{\theta}} \approx \frac{1}{R_{\theta}} \left| \frac{\chi[\Omega_F + \delta]}{\chi[\Omega_F - \delta]} \right|^2 \frac{\langle \delta F_+^2 \rangle}{\langle \delta F_-^2 \rangle}, \quad (8)$$

is directly related to the magnitude of the asymmetry R_{θ} .

In fig. 5, we show the result of an experiment that evidences the role of quantum correlations in enhancing the signal-to-noise ratio for external force estimation. The auxiliary laser (at 850 nm) is used to apply two coherent radiation pressure forces on the oscillator, nominally balanced in intensity ($\langle \delta F_+^2 \rangle / \langle \delta F_-^2 \rangle \approx 1$) and symmetric with respect to mechanical resonance ($\Omega_F \approx \Omega_m$), as shown in fig. 5A. Performing a variational measurement as before, the homodyne angle θ is varied, while the ratio of the signal-to-noises of the two forces is measured. Figure 5B shows this ratio as a function of the homodyne angle. For the case where the forces

are precisely balanced, eq. (8) predicts that quantum correlations lead to an improvement in the signal-to-noise ratio between the two forces, quantitatively given by R_{θ} . As shown in fig. 5B, we observe a modest improvement in the signal-to-noise ratio (by about 3%) on one side of the mechanical resonance compared to the other. In the absence of such correlations, $R_{\theta} \approx 1$, limited by any residual asymmetry due to the mechanical susceptibility; the resulting classical prediction is shown as a red dashed curve in fig. 5B. The closer agreement of the data with the full quantum mechanical prediction suggests that the signal-to-noise improvement observed in our experiment is due to quantum correlations in the meter beam.

In future room-temperature experiments, where the back-action force is the dominant contaminant in the estimation of weak external forces, variational measurements, as demonstrated here, could beat the standard quantum limit for force estimation via conventional detection.

Acknowledgements: All samples are fabricated at the CMi (Center for MicroNanoTechnology) at EPFL. Research is funded by an ERC Advanced Grant (QuREM), a Marie Curie Initial Training Network Cavity Quantum Optomechanics, the Swiss National Science Foundation, and through support from the NCCR of Quantum Engineering (QSIT). D. J. W. acknowledges support from the European Commission through a Marie Curie Fellowship (IIF Project No. 331985)

-
- [1] V. Braginsky and A. Manukin, *Sov. Phys. JETP* **25**, 653 (1967).
[2] C. M. Caves, *Phys. Rev. Lett.* **45**, 75 (1980).
[3] V. Braginsky and F. Khalili, *Quantum Measurements* (Cambridge University Press, 1995).
[4] A. A. Clerk, M. H. Devoret, S. M. Girvin, F. Marquardt, and R. J. Schoelkopf, *Rev. Mod. Phys.* **82**, 1155 (2010).
[5] C. Fabre, M. Pinard, S. Bourzeix, A. Heidmann, E. Giacobino, and S. Reynaud, *Phys. Rev. A* **49**, 1337 (1994).
[6] S. Mancini and P. Tombesi, *Phys. Rev. A* **49**, 4055 (1994).
[7] S. P. Vyatchanin and E. A. Zubova, *Phys. Lett. A* **201**, 269 (1995).
[8] H. J. Kimble, Y. Levin, A. B. Matsko, K. S. Thorne, and S. P. Vyatchanin, *Phys. Rev. D* **65**, 022002 (2001).
[9] A. Buonanno and Y. Chen, *Phys. Rev. D* **64**, 042006 (2001).
[10] M. Aspelmeyer, T. J. Kippenberg, and F. Marquardt, *Rev. Mod. Phys.* **86**, 1391 (2014).
[11] T. P. Purdy, R. W. Peterson, and C. A. Regal, *Science* **339**, 801 (2013).
[12] D. J. Wilson, V. Sudhir, N. Piro, R. Schilling, A. Ghadimi, and T. J. Kippenberg, *Nature* **524**, 325 (2015).
[13] J. D. Teufel, F. Lecocq, and R. W. Simmonds, *Phys. Rev. Lett.* **116**, 013602 (2016).
[14] A. H. Safavi-Naeini, J. Chan, J. T. Hill, T. P. M. Alegre, A. Krause, and O. Painter, *Phys. Rev. Lett.* **108**, 033602 (2012).
[15] F. Y. Khalili, H. Miao, H. Yang, A. H. Safavi-Naeini, O. Painter, and Y. Chen, *Phys. Rev. A* **86**, 033840 (2012).
[16] A. Weinstein, C. Lei, E. Wollman, J. Suh, A. Metelmann, A. Clerk, and K. Schwab, *Phys. Rev. X* **4**, 041003 (2014).
[17] T. P. Purdy, P.-L. Yu, N. S. Kampel, R. W. Peterson, K. Cicak, R. W. Simmonds, and C. A. Regal, *Phys. Rev. A* **92**, 031802 (2015).
[18] M. Underwood, D. Mason, D. Lee, H. Xu, L. Jiang, A. B. Shkarin, K. Børkje, S. M. Girvin, and J. G. E. Harris, *Phys. Rev. A* **92**, 061801 (2015).
[19] V. Sudhir, D. Wilson, R. Schilling, H. Schütz, A. Ghadimi, A. Nunnenkamp, and T. J. Kippenberg, *arXiv:1602.05942* (2016).
[20] D. W. C. Brooks, T. Botter, S. Schreppler, T. P. Purdy, N. Brahm, and D. M. Stamper-Kurn, *Nature* **488**, 476 (2012).
[21] A. H. Safavi-Naeini, S. Gröblacher, J. T. Hill, J. Chan, M. Aspelmeyer, and O. Painter, *Nature* **500**, 185 (2013).
[22] W. Nielsen, Y. Tsaturyan, C. B. Moller, E. S. Polzik, and A. Schliesser, *arXiv:1605.06541* (2016).
[23] P. Verlot, A. Tavernarakis, T. Briant, P.-F. Cohadon, and A. Heidmann, *Phys. Rev. Lett.* **104**, 133602 (2010).
[24] T. P. Purdy, K. E. Grutter, K. Srinivasan, and J. M. Taylor, *arXiv:1605.05664* (2016).
[25] R. Schilling, H. Schütz, A. Ghadimi, V. Sudhir, D. Wilson, and T. Kippenberg, *Phys. Rev. Applied* **5**, 054019 (2016).
[26] K. Børkje, A. Nunnenkamp, B. Zwickl, C. Yang, J. Harris, and S. Girvin, *Phys. Rev. A* **82**, 13818 (2010).
[27] J. B. Clark, F. Lecocq, R. W. Simmonds, J. Aumentado, and J. D. Teufel, *Nature Physics* **12**, 683 (2016).
[28] V. Giovannetti, S. Lloyd, and L. Maccone, *Science* **306**, 1330 (2004).
[29] C. M. Caves, M. Zimmermann, K. S. Thorne, and R. W. Drever, *Rev. Mod. Phys.* **52**, 341 (1980).
[30] N. S. Kampel, R. W. Peterson, R. Fischer, P.-L. Yu, K. Cicak, R. W. Simmonds, K. W. Lehnert, and C. A. Regal, *arXiv:1607.06831* (2016).
[31] C. Gardiner and M. Collett, *Phys. Rev. A* **31**, 3761 (1985).
[32] A. A. Clerk, M. H. Devoret, S. M. Girvin, F. Marquardt, and R. J. Schoelkopf, *Rev. Mod. Phys.* **82**, 1155 (2010).
[33] P. Cohadon, A. Heidmann, and M. Pinard, *Phys. Rev. Lett.* **83**,

- 3174 (1999).
- [34] P. R. Saulson, *Phys. Rev. D* **42**, 2437 (1990).
 - [35] G. I. González and P. R. Saulson, *Phys. Lett. A* **201**, 12 (1995).
 - [36] M. Kajima, N. Kusumi, S. Moriwaki, and N. Mio, *Phys. Lett. A* **264**, 251 (1999).
 - [37] L. B. Mercer, *J. Lightwave Tech.* **9**, 485 (1991).
 - [38] V. B. Braginsky, M. L. Gorodetsky, and S. P. Vyatchanin, *Phys. Lett. A* **264**, 1 (1999).
 - [39] V. B. Braginsky, M. L. Gorodetsky, and S. P. Vyatchanin, *Phys. Lett. A* **271**, 303 (2000).
 - [40] G. E. Hudson, *Phys. Rev.* **63**, 46 (1943).
 - [41] J. Zemanek and I. Rudnick, *J. Acoust. Soc. Am.* **33**, 1283 (1961).
 - [42] S. Harun, K. Lim, C. Tio, K. Dimiyati, and H. Ahmad, *Optik* **124**, 538 (2013).
 - [43] R. M. Shelby, M. D. Levenson, and P. W. Bayer, *Phys. Rev. B* **31**, 5244 (1985).

Supplementary Information

CONTENTS

A. Theoretical model for optomechanically induced quantum correlations	8
1. Effect of excess laser noise and detuning	9
B. Experimental details	11
1. Experimental platform	11
2. Measurement setup	11
3. Data analysis	12
4. Role of mechanical susceptibility	14
5. Laser noise	14
6. Excess detection noise due to taper vibrations	15
C. Quantum-enhanced force sensitivity	16
1. Correlation enhanced thermal force sensing	17
2. Correlation enhanced external force sensing	17

Appendix A: Theoretical model for optomechanically induced quantum correlations

We consider here an optomechanical system consisting of an optical cavity, whose intracavity field is described by the amplitude $a(t)$, dispersively coupled to a mechanical oscillator, whose position is described by $x(t)$. Following standard linearization procedure [10], the fluctuations in either variable, denoted δa and δx respectively, satisfy the equations of motion,

$$\begin{aligned}\delta\dot{a} &= \left(i\Delta - \frac{\kappa}{2}\right)\delta a + iG\bar{a}\delta x + \sqrt{\eta_c\kappa}\delta a_{in} + \sqrt{(1-\eta_c)\kappa}\delta a_0 \\ \delta\ddot{x} + \Gamma_m\delta\dot{x} + \Omega_m^2\delta x &= \delta F_{th} + \hbar G\bar{a}(\delta a + \delta a^\dagger).\end{aligned}\tag{A1}$$

Here G is the cavity frequency pull parameter, the dispersive optomechanical coupling strength. The noise variables $\delta a_{in,0}$ describe the fluctuations in the cavity input at the coupling port and the port modelling internal losses. The cavity coupling efficiency $\eta_c = \kappa_{ex}/\kappa$, describes the relative strength of the external coupling port. The steady state intracavity photon number, $n_c = \bar{a}^2$ is given by,

$$n_c = \frac{4\eta_c}{\kappa} \frac{P_{in}/\hbar\omega_L}{1 + 4\Delta^2/\kappa^2},$$

where P_{in} is the injected probe power at optical frequency ω_L .

In the experimentally relevant situation of resonant probing ($\Delta \approx 0$) and bad cavity limit ($\Omega_m \gg \kappa$), the equation of motion for the cavity field in eq. (A1) assumes the form,

$$\delta a[\Omega] \approx \frac{2ig}{\kappa}\delta z[\Omega] + \frac{2}{\sqrt{\kappa}} \left(\sqrt{\eta_c}\delta a_{in}[\Omega] + \sqrt{1-\eta_c}\delta a_0[\Omega] \right),$$

where we have introduced the normalized position, $\delta z := \delta x/x_{zp}$, and the optomechanical coupling rate, $g := G\bar{a}x_{zp}$; $x_{zp} = \sqrt{\hbar/2m\Omega_m}$ is the zero-point variance in the position of the mechanical oscillator of effective mass m . Using the input-output relation [31], $\delta a_{out} = \delta a_{in} - \sqrt{\eta_c\kappa}\delta a$, the transmitted fluctuations,

$$\delta a_{out}[\Omega] = (1 - 2\eta_c)\delta a_{in}[\Omega] - 2\sqrt{\eta_c(1-\eta_c)}\delta a_0[\Omega] - i\sqrt{\eta_c C\Gamma_m}\delta z[\Omega],\tag{A2}$$

carries information regarding the total mechanical motion δz consisting of the thermal motion and the quantum back-action driven motion, i.e.,

$$\delta z[\Omega] = \delta z_{th}[\Omega] + \delta z_{QBA}[\Omega].$$

In eq. (A2), we have also introduced the multi-photon cooperativity of the optomechanical system:

$$C := \frac{4g^2}{\kappa\Gamma_m}.$$

The back-action motion is given by,

$$\delta z_{\text{BA}}[\Omega] = \sqrt{2C\Gamma_m} \frac{\hbar\chi[\Omega]}{x_{\text{zp}}^2} \left(\sqrt{\eta_c} \delta q_{\text{in}}[\Omega] + \sqrt{1-\eta_c} \delta q_0[\Omega] \right), \quad (\text{A3})$$

where $\delta q_{\text{in},0}$ are the amplitude quadrature fluctuations from the two cavity input ports, and

$$\chi[\Omega] = m^{-1}(-\Omega^2 + \Omega_m^2 - i\Omega\Gamma_m)^{-1}, \quad (\text{A4})$$

is the susceptibility of the mechanical oscillator position to applied force. Note that here and henceforth, we define the quadratures of the optical field δa are defined by,

$$\delta q(t) = \frac{1}{\sqrt{2}} (\delta a(t) + \delta a^\dagger(t)), \quad \delta p(t) = \frac{1}{i\sqrt{2}} (\delta a(t) - \delta a^\dagger(t)). \quad (\text{A5})$$

Inserting eq. (A3) in eq. (A2), the two quadratures of the cavity transmission are,

$$\begin{aligned} \delta q_{\text{out}}[\Omega] &= (1 - 2\eta_c)\delta q_{\text{in}}[\Omega] - 2\sqrt{\eta_c(1-\eta_c)}\delta q_0[\Omega] \\ \delta p_{\text{out}}[\Omega] &= (1 - 2\eta_c)\delta p_{\text{in}}[\Omega] - 2\sqrt{\eta_c(1-\eta_c)}\delta p_0[\Omega] \\ &\quad - \sqrt{2\eta_c C\Gamma_m} \left[\delta z_{\text{th}}[\Omega] + \sqrt{2C\Gamma_m} \frac{\hbar\chi[\Omega]}{x_{\text{zp}}^2} \left(\sqrt{2\eta_c} \delta q_{\text{in}}[\Omega] + \sqrt{2(1-\eta_c)}\delta q_0[\Omega] \right) \right]. \end{aligned} \quad (\text{A6})$$

For a general quadrature at angle θ , defined by,

$$\delta q_{\text{out}}^\theta[\Omega] := \delta q_{\text{out}}[\Omega] \cos \theta + \delta p_{\text{out}}[\Omega] \sin \theta,$$

it follows that,

$$\begin{aligned} \langle \delta q_{\text{out}}^\theta[\Omega] \delta q_{\text{out}}^\theta[-\Omega] \rangle &= \cos^2 \theta \langle \delta q_{\text{out}}[\Omega] \delta q_{\text{out}}[-\Omega] \rangle \\ &\quad + \sin^2 \theta \langle \delta p_{\text{out}}[\Omega] \delta p_{\text{out}}[-\Omega] \rangle \\ &\quad + \sin(2\theta) \text{Re} \langle \delta q_{\text{out}}[\Omega] \delta p_{\text{out}}[-\Omega] \rangle. \end{aligned} \quad (\text{A7})$$

The homodyne photocurrent spectrum is related to this correlator via,

$$\bar{S}_{II}^{\theta, \text{hom}}[\Omega] \cdot 2\pi\delta[0] \propto \bar{S}_{qq}^{\theta, \text{out}}[\Omega] \cdot 2\pi\delta[0] = \frac{1}{2} \langle \{ \delta q_{\text{out}}^\theta[\Omega], \delta q_{\text{out}}^\theta[-\Omega] \} \rangle. \quad (\text{A8})$$

Inserting eq. (A6) in eq. (A7), and using the above definition, we arrive at the homodyne photocurrent spectrum (normalized to electronic shot noise),

$$\bar{S}_{II}^{\theta, \text{hom}}[\Omega] = 1 + \frac{4\eta C\Gamma_m}{x_{\text{zp}}^2} \left(\bar{S}_{xx}[\Omega] \sin^2 \theta + \frac{\hbar}{2} \sin(2\theta) \text{Re} \chi[\Omega] \right). \quad (\text{A9})$$

Note that henceforth (as in the main manuscript) photocurrent spectra are implicitly normalized to shot noise. Using the fluctuation-dissipation theorem [32] to relate the thermal and back-action force noise to mean phonon occupations n_{th} and n_{BA} respectively, the spectral density of the total motion,

$$\bar{S}_{xx}[\Omega] = \frac{4x_{\text{zp}}^2 (\Omega_m\Gamma_m)^2 (n_{\text{th}} + n_{\text{QBA}} + \frac{1}{2})}{\Gamma_m (\Omega^2 - \Omega_m^2)^2 + (\Omega\Gamma_m)^2}, \quad (\text{A10})$$

where, $n_{\text{th}} \approx k_B T / \hbar\Omega_m$ is the average thermal occupation, and, $n_{\text{QBA}} = C = C_0 n_c$ is the average occupation due to (quantum) back-action arising from vacuum fluctuations in the input amplitude quadrature.

1. Effect of excess laser noise and detuning

In addition to vacuum fluctuations in the input amplitude quadrature, classical fluctuations in the amplitude quadrature can lead to phase-amplitude correlations in the cavity transmission. Additionally, detuning deviations causing a finite Δ/κ can transduce classical phase fluctuations in the input to excess phase-amplitude correlations in the output.

In order to analyse the two possible classical contributions on the same footing, we consider the quadratures of the cavity transmission, $\delta q_{\text{out}}, \delta p_{\text{out}}$ for the case of a finite detuning $|\Delta| \ll \kappa$. In this regime, eq. (A6) contains corrections of order Δ/κ , viz.,

$$\begin{aligned}\delta q_{\text{out}}[\Omega] &= (1 - 2\eta_c)\delta q_{\text{in}}[\Omega] - 2\sqrt{\eta_c(1 - \eta_c)}\delta q_0[\Omega] \\ &\quad + \frac{2\Delta}{\kappa} \left(\sqrt{2\eta_c C\Gamma_m}\delta z[\Omega] + 2\eta_c\delta p_{\text{in}}[\Omega] + 2\sqrt{\eta_c(1 - \eta_c)}\delta p_0[\Omega] \right) \\ \delta p_{\text{out}}[\Omega] &= (1 - 2\eta_c)\delta p_{\text{in}}[\Omega] - 2\sqrt{\eta_c(1 - \eta_c)}\delta p_0[\Omega] - \sqrt{2\eta_c C\Gamma_m}\delta z[\Omega] \\ &\quad - \frac{2\Delta}{\kappa} \left(2\eta_c\delta q_{\text{in}}[\Omega] + 2\sqrt{\eta_c(1 - \eta_c)}\delta q_0[\Omega] \right),\end{aligned}\tag{A11}$$

where the total motion $\delta z = \delta z_{\text{th}} + \delta z_{\text{BA}}$, with,

$$\begin{aligned}\delta z_{\text{BA}}[\Omega] &= \sqrt{2C\Gamma_m} \frac{\hbar}{x_{\text{zfp}}^2} \left[\left(\sqrt{\eta_c}\delta q_{\text{in}}[\Omega] + \sqrt{1 - \eta_c}\delta q_0[\Omega] \right) \right. \\ &\quad \left. + 4i \frac{\Omega\Delta}{\kappa^2} \left(\sqrt{\eta_c}\delta p_{\text{in}}[\Omega] + \sqrt{1 - \eta_c}\delta p_0[\Omega] \right) \right],\end{aligned}\tag{A12}$$

the motion induced by the quantum and the classical fluctuations in the input laser field. Excess noise in the input amplitude and phase quadratures is modelled by white noise with intensity C_{qq} and C_{pp} respectively, so that,

$$\bar{S}_{qq}^{\text{in}}[\Omega] = \frac{1}{2} + C_{qq}, \quad \bar{S}_{pp}^{\text{in}}[\Omega] = \frac{1}{2} + C_{pp}.$$

Using eqs. (A11) and (A12) in the definition of the homodyne spectrum (eq. (A8)) to leading order in Δ/κ , the shot-noise normalized balanced homodyne spectrum is:

$$\begin{aligned}\bar{S}_{II}^{\theta, \text{hom}}[\Omega] &\approx 1 + \frac{4\eta C\Gamma_m}{x_{\text{zfp}}^2} \left[\left(\bar{S}_{xx}^{\text{th+QBA}}[\Omega] + \bar{S}_{xx}^{\text{CBA,q}}[\Omega] + \bar{S}_{xx}^{\text{CBA,p}}[\Omega] \right) \sin(\theta')^2 + \frac{\hbar}{2} \sin(2\theta') \text{Re } \chi[\Omega] + \right. \\ &\quad \left. + \hbar \sin(2\theta') \sqrt{\eta_c}(1 - 2\eta_c)C_{qq} \text{Re } \chi[\Omega] + 2\hbar \sin(\theta')^2 \sqrt{\eta_c}(1 - 2\eta_c) \frac{4\Omega_m\Delta}{\kappa^2} C_{pp} \text{Im } \chi[\Omega] \right],\end{aligned}\tag{A13}$$

where $\theta' \approx \theta - 4\Delta/\kappa$ is the quadrature angle rotated by the cavity. The effect of excess noise is two-fold. Firstly, classical amplitude (phase) noise C_{qq} (C_{pp}) causes additional classical back-action motion $\bar{S}_{xx}^{\text{CBA,q}}$ ($\bar{S}_{xx}^{\text{CBA,p}}$), leading to excess back-action occupations,

$$n_{\text{CBA,q}} = C_0 n_c C_{qq}, \quad n_{\text{CBA,p}} = C_0 n_c \left(\frac{4\Omega_m\Delta}{\kappa^2} \right)^2 C_{pp}.\tag{A14}$$

Secondly, classical amplitude noise, and phase noise transduced via finite detuning, establish excess correlations, as can be seen from the last two terms in the eq. (A13). It is important to note that the contribution of excess phase noise C_{pp} to the measured homodyne signal is effectively suppressed for the current experimental parameters as $\Delta \cdot \Omega_m/\kappa^2 = \mathcal{O}(10^{-4})$. Finally, when laser noise is insignificant, the role of a residual detuning from the cavity, i.e. $\Delta \neq 0$, is to rotate the detected quadrature by an angle $\arctan(4\Delta/\kappa)$, without leading to any artificial asymmetry.

Appendix B: Experimental details

1. Experimental platform

The device measured in this work consists of an SiO_2 whispering gallery mode microdisk with a high-stress Si_3N_4 nanobeam centered in the near-field of the microdisk. The sample has been fabricated by a monolithic wafer-scale process that utilizes a sacrificial layer to define an ~ 50 nm gap between the microdisk and nanobeam, as detailed in [25]. Similar devices have also been used for recent cryogenic experiments [12, 19]. However, in contrast to those devices, in the devices used here both the mechanical and optical resonator shapes are defined by electron-beam lithography. The bare microdisks exhibit very high finesse of $\sim 10^5$ – nearly an order of magnitude higher than microdisks produced by photo-lithography. However, in this work we do not access this high finesse regime when the nanobeam is placed in the near-field of the disk. We attribute this to the 80 nm thickness of the Si_3N_4 , which is conjectured to lead to excessive scattering and/or waveguiding. The microdisk is $40\ \mu\text{m}$ in diameter, ~ 350 nm thick, and has a gently sloping sidewall of $\sim 10^\circ$ which results from the use of thin photoresist during the wet-etching process.

In previous work [12, 19] the mechanical resonator was formed by a beam with a homogeneous transverse profile. However, the present device has been designed with a central defect that allows for increased overlap with the optical mode while minimizing the effective mass ($m_{\text{eff}} \approx 1.94$ pg). The optical mode of the microdisk samples approximately $9\ \mu\text{m}$ of the beam at its center (see [25]), however we utilize a defect that is tapered within the sampling region as this resulted in lower optical loss and overall higher C_0 than longer defects. This effect may be attributed to the reduced scattering loss on account of a softer dielectric boundary seen by the optical mode. Figure 6B shows the defect geometry and the effect of defect length on the effective mass of the fundamental out-of-plane mode. The beam is $70\ \mu\text{m}$ long and consists of a narrow (200 nm) beam with a wider (400 nm) rectangular defect at the center which tapers linearly into the thin beam at an angle of $\sim 12^\circ$. The defect length of the device used in this paper is $5\ \mu\text{m}$, which exhibits an effective mass only 11% larger than that of a standard 200 nm wide beam.

As shown in Figure 6A, two short beams of Si_3N_4 with dimensions $20 \times 0.2 \times 0.08\ \mu\text{m}$ are also placed across the channel on either side of the microdisk to support the tapered optical fiber and increase the overall mechanical stability of the experiment.

2. Measurement setup

The essential layout of the experiment is shown in fig. 7. The sample is placed in a high vacuum chamber, at a pressure of $\sim 10^{-7}$ mbar, and room temperature. Light is coupled in and out of the microdisk cavity using a tapered optical fiber, the position of which is adjusted using piezo actuators to achieve critical coupling into the cavity (i.e. $\eta_c \approx 0.5$).

Two lasers are employed in the experiment – a TiSa laser (MSquared Solstis) with wavelength centered around 780 nm which is the meter beam, and an auxiliary 850 nm external cavity diode laser (NewFocus Velocity) which is the feedback beam. Both beams are combined before the cavity and separated after it using dichroic beamsplitters. The feedback beam is detected on an

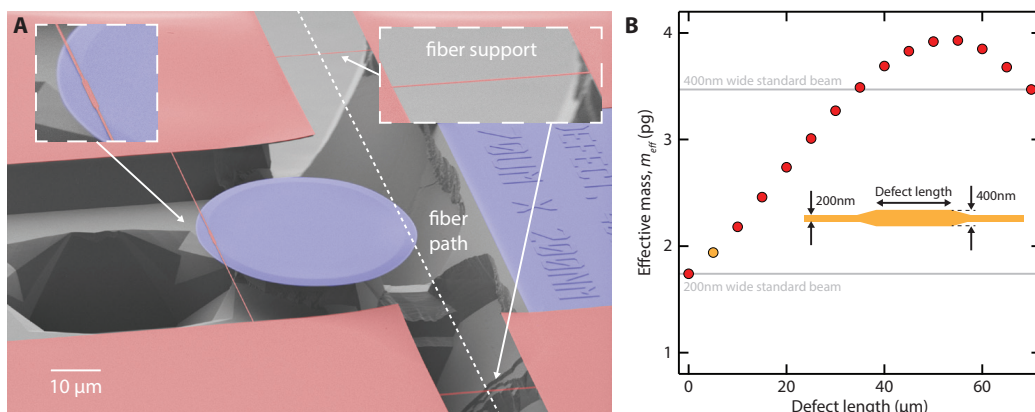


FIG. 6. (A) False colored scanning electron micrograph of the device design used in this work. Si_3N_4 is indicated in red and SiO_2 in blue. (B) Finite element calculation of effective mass for defect beam design, as a function of the defect length. The data point in orange indicates the defect length ($5\ \mu\text{m}$) of the experimental device; see text for details.

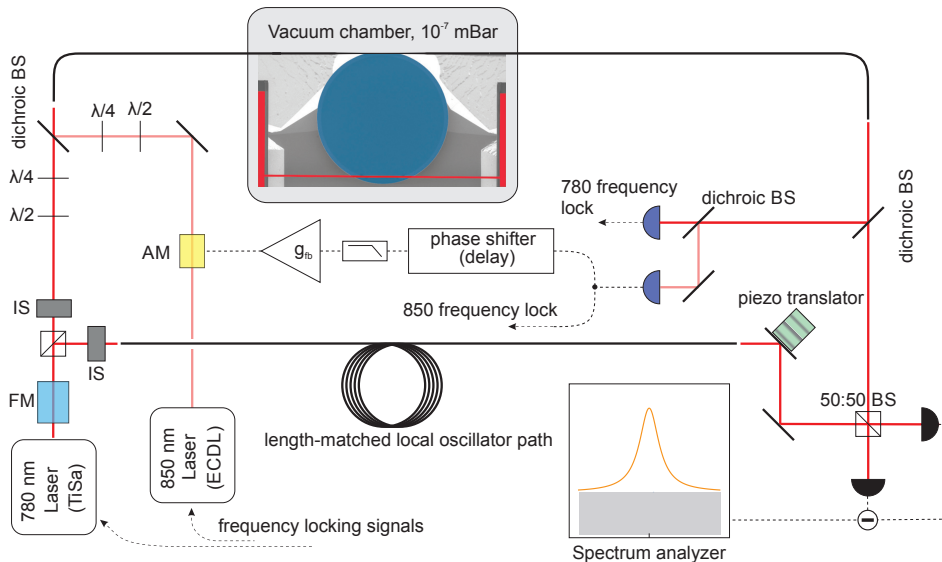


FIG. 7. Schematic of the experimental setup. Abbreviations: AM – amplitude modulator, FM – frequency modulator, BS – beam splitter, IS – intensity stabilizer.

avalanche photodetector (APD), while the meter beam is fed into a length- and power-balanced homodyne detector. A small portion of the meter beam – stray reflection from the dichroic beam-splitter – is directed onto an APD.

Both lasers are actively locked to their independent cavity resonances using the APD signal. For the meter beam, a lock on cavity resonance ($|\Delta| \lesssim 0.1 \cdot \kappa$) is implemented using the Pound-Drever-Hall technique. For the feedback beam, a part of the APD signal is used directly to implement a lock red-detuned from cavity resonance.

The other part of the feedback beam APD signal is used to perform moderate feedback cooling of the mechanical oscillator. Specifically, the photosignal is amplified, low-pass filtered and phase-shifted, before using it to amplitude modulate the same laser. As in conventional cold damping [33], the phase-shift in the feedback loop is adjusted to synthesise an out-of-phase radiation pressure force that damps the mechanical oscillator. At the nominal feedback laser power of $5 \mu\text{W}$, a damping rate of 1 kHz is realized; the associated increase in the mechanical decoherence rate due to injected imprecision noise was measured to be below 5%.

The path length difference of the homodyne interferometer is actively stabilized using a two-branch piezo translation system. Demodulation of the homodyne signal at PDH frequency also produced interference fringes suitable for locking the homodyne angle near the amplitude quadrature (i.e. $\theta = 0$). The residual homodyne angle fluctuations could be estimated $\theta_{\text{RMS}} \lesssim 1^\circ \approx 0.017 \text{ rad}$, inferred from the suppression of thermomechanical signal-to-noise ratio on amplitude quadrature of $\approx 10^{-4}$ compared to the phase quadrature. An offset DC voltage is applied to the homodyne error signal for deterministic choice of detection quadrature.

Since the feedback cooling exclusively relies on the auxiliary diode laser, the homodyne measurements on the 780 nm meter beam are completely out-of-loop and does not contain electronically-induced correlations.

3. Data analysis

In each experimental run, corresponding to the data shown in one panel of Figure 3 of the main text, the meter laser is locked to cavity resonance at fixed input power, and a series of homodyne photocurrent spectra are taken at various settings of the homodyne angle θ . From independently measured mechanical and optical parameters of the sample, together with the known input power, the homodyne detection efficiency is inferred in each run by the thermomechanical signal-to-shot-noise ratio (shot noise level was measured by blocking the signal interferometer arm). To account for a small quadrature rotation by the cavity the nominal $\theta = 0$ quadrature was inferred from the minimum in the transduction of thermomechanical noise.

In order to experimentally access the asymmetry ration R_θ discussed in the main text, R_θ is estimated from an integral over a finite bandwidth $\Delta\Omega$, i.e.,

$$R_\theta = \frac{\int_{\Omega_m + \delta - \Delta\Omega/2}^{\Omega_m + \delta + \Delta\Omega/2} \bar{S}_{II}^\theta[\Omega] d\Omega}{\int_{\Omega_m - \delta - \Delta\Omega/2}^{\Omega_m - \delta + \Delta\Omega/2} \bar{S}_{II}^\theta[\Omega] d\Omega}. \quad (\text{B1})$$

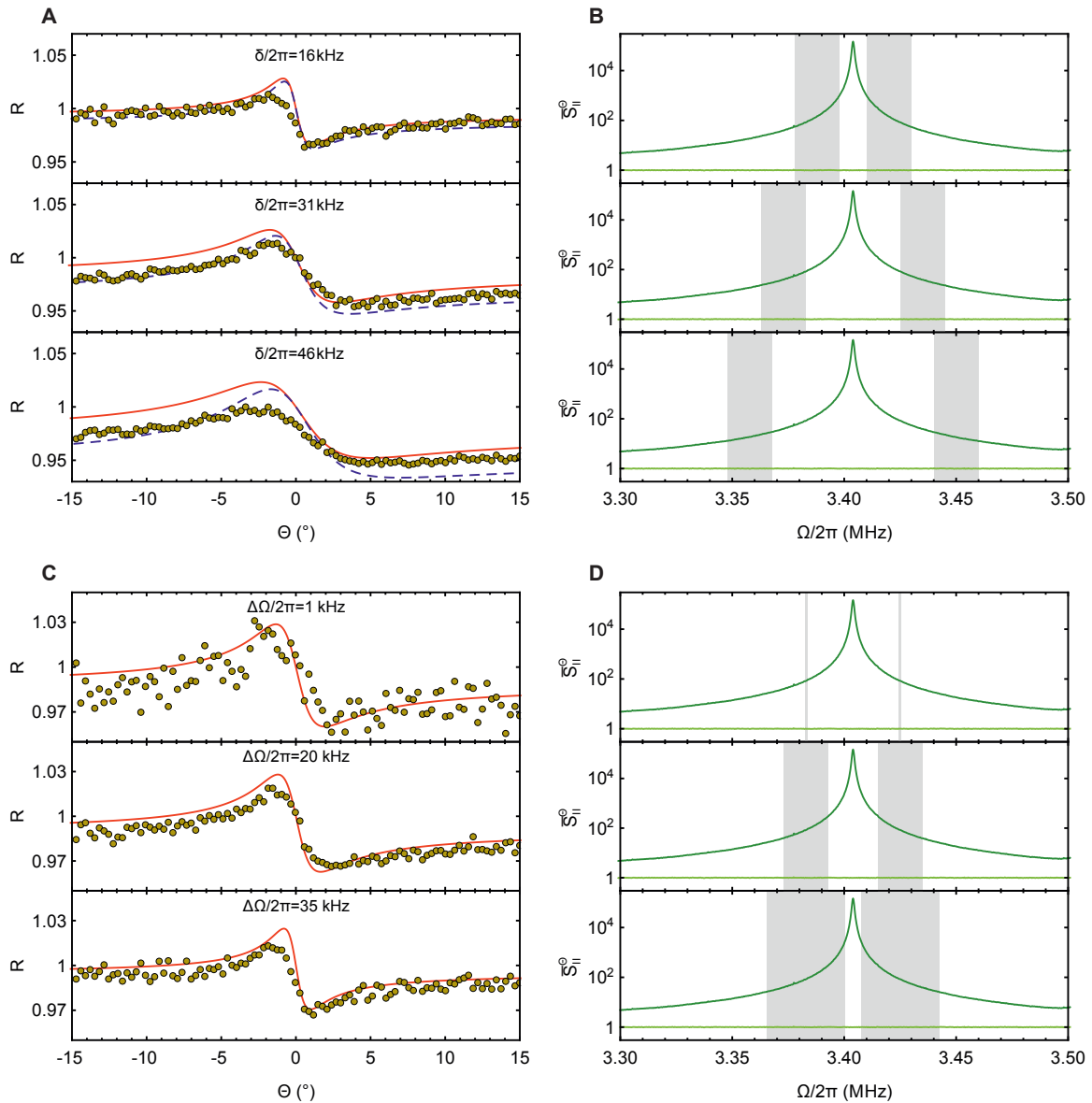


FIG. 8. (A,C) Illustration of the variation of the experimental asymmetry ratio $R(\theta)$ for different offsets δ at fixed integration bandwidth $\Delta\Omega\pi = 20$ kHz (A) and for different integration bandwidths $\Delta\Omega$ at fixed offset $\delta/2\pi = 21$ kHz (C). Solid red and dashed blue curves show theoretical predictions corresponding to the viscous (eq. (B4)) and structural (eq. (B5)) damping models of the oscillator dissipation. Deviation of the mechanical susceptibility from the former results in $R(\theta)$ being not perfectly asymmetric with degree of distortion increasing with δ . (B,D) Plots show the integration bands used for calculation of the $R(\theta)$ on the left (shaded gray regions). Dark green is a mechanical spectrum at an intermediate homodyne quadrature and light green is the local oscillator trace showing the shot noise level. The data was taken at $P_{\text{in}} = 25\mu W$.

Theoretically, there is some freedom in the choice of the detuning offset δ and integration bandwidth $\Delta\Omega$, since the relative contribution of the quantum interference term to the detected signal is maximum within a broad range of detunings $\Gamma_{\text{eff}} \ll \delta \ll 2\Gamma_m\sqrt{\eta C n_{\text{th}}}$; here $\Gamma_{\text{eff}} \approx 2\pi \cdot 1$ kHz is the effective damping rate due to feedback. For typical experimental conditions in this work 1 kHz $\ll \delta/2\pi \ll 500$ kHz. Figure 8 shows the ratio R_θ extracted for various choices of the detuning offset and integration bandwidth. Figure 3 of the main manuscript depicts data extracted for the choice $\delta = 2\pi \cdot 21$ kHz and $\Delta\Omega = 2\pi \cdot 20$ kHz.

In the demonstration of external force estimation in the main manuscript, the signal-to-noise ratio for the applied force δF_{ext} is defined by,

$$\text{SN}_{\pm}^{\theta} \equiv \bar{S}_{II}^{\theta}[\Omega_F \pm \delta] / \bar{S}_{II}[\Omega_F \pm \delta]|_{\delta F_{\text{ext}}=0}; \quad (\text{B2})$$

i.e., the signal is the photocurrent noise at the frequencies where the force is applied ($\Omega_F \pm \delta$), while the noise is the photocurrent noise at the same frequencies without the force. Practically, we estimate both contributions from finite bandwidth integrals

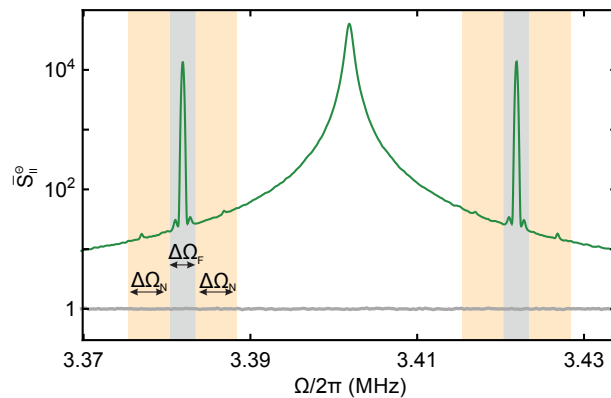


FIG. 9. Integration bands used in the definition of the signal-to-noise ratio SN^θ in the main manuscript. The signal bands are shaded gray ($\Delta\Omega_F = 3$ kHz), the bands for noise estimation are shaded orange ($\Delta\Omega_N = 5$ kHz).

over the relevant part of the photocurrent spectrum: for the signal, the photocurrent signal is integrated over a finite bandwidth $\Delta\Omega_F$ around the applied force, while to estimate the noise, we choose to take averages of the photocurrent spectrum over finite bandwidth $\Delta\Omega_N$, on either side of the applied force, without turning off the force. Specifically,

$$\text{SN}_{\pm}^\theta = \int_{\Omega_F \pm \delta - \Delta\Omega_F/2}^{\Omega_F \pm \delta + \Delta\Omega_F/2} \bar{S}_{II}^\theta[\Omega] d\Omega \left/ \frac{1}{2} \left(\int_{\Omega_F \pm \delta + \delta\Omega_N - \Delta\Omega_N/2}^{\Omega_F \pm \delta + \delta\Omega_N + \Delta\Omega_N/2} \bar{S}_{II}^\theta[\Omega] d\Omega + \int_{\Omega_F \pm \delta - \delta\Omega_N - \Delta\Omega_N/2}^{\Omega_F \pm \delta - \delta\Omega_N + \Delta\Omega_N/2} \bar{S}_{II}^\theta[\Omega] d\Omega \right) \right. . \quad (\text{B3})$$

The integration bands used for the Figure 5 in the main text are shown in fig. 9.

4. Role of mechanical susceptibility

In practice however, for detunings from the mechanical resonance $\delta/2\pi > 30$ kHz analysis is sensitive to possible deviations of the mechanical oscillator susceptibility from a simple velocity damped model (eq. (A4)),

$$\chi_{\text{velo}}[\Omega] = \frac{1/m}{(\Omega_m^2 - \Omega^2) - i\Omega\Gamma_m} . \quad (\text{B4})$$

For example, a model of the mechanical oscillator taking into account inelastic structural damping, described by the susceptibility [34–36],

$$\chi_{\text{struc}}[\Omega] = \frac{1/m}{(\Omega_m^2 - \Omega^2) - i(\Omega\Gamma_m + \Omega_m^2\phi[\Omega])} \quad (\text{B5})$$

introduces a distortion in the otherwise anti-symmetric function R_θ , depending on the anelastic loss angle $\phi[\Omega]$. For a large class of materials, $\phi[\Omega] \approx Q^{-1}$, and the distortion increases with increasing detuning from mechanical resonance, δ . For simplicity we chose a band relatively close to the mechanical resonance, the variation of the data analysis result for various choices of the integration band is shown in fig. 8.

In order to extract the scaling of the maximum asymmetry ΔR , shown in Figure 4 of the main manuscript, the experimental dependences R_θ were transformed by correcting for the contribution due to non-Lorentzian mechanical susceptibility

$$R_{\theta \text{ corr}} = R_\theta \times \int_{\Omega_m - \delta - \Delta\Omega/2}^{\Omega_m - \delta + \Delta\Omega/2} |\chi[\Omega]|^2 d\Omega \left/ \int_{\Omega_m + \delta - \Delta\Omega/2}^{\Omega_m + \delta + \Delta\Omega/2} |\chi[\Omega]|^2 d\Omega \right. . \quad (\text{B6})$$

5. Laser noise

A MSquared Solstis Ti:Sa laser was used for the measurements presented in the manuscript. The amplitude noise of the laser was characterized via direct photo-detection. In a frequency band 3 MHz wide around the mechanical frequency, $\Omega_m = 2\pi \cdot 3.4$ MHz at the highest employed power $50 \mu\text{W}$ the classical amplitude noise level was $< 1\%$ of the shot noise (see

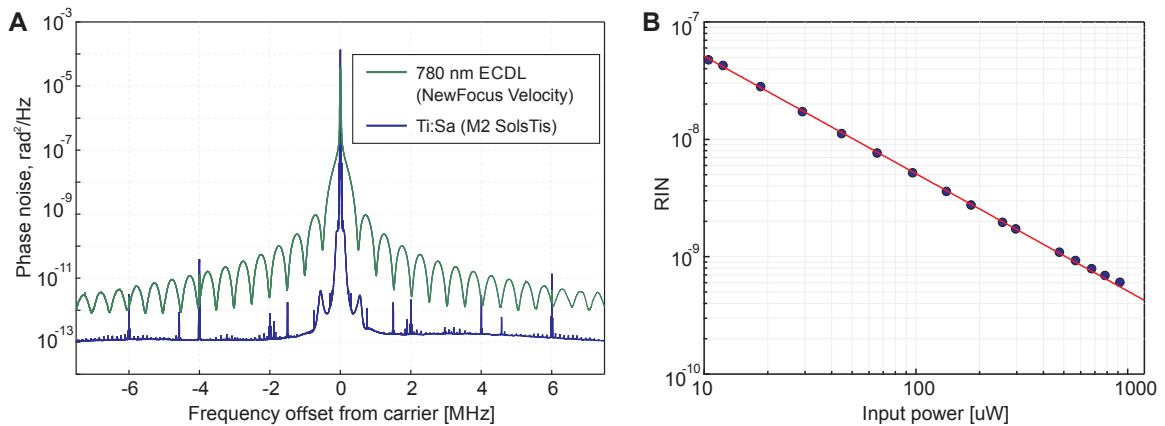


FIG. 10. (A) Phase noise about the carrier, measured using an imbalanced Mach-Zehnder interferometer (self-heterodyning). Blue color shows the measurement for the employed Ti:Sa, whose phase noise contribution can be estimated to be $\leq 2 \cdot 10^{-13} \text{ rad}^2/\text{Hz}$ around the mechanical frequency $\approx 3.4 \text{ MHz}$, corresponding to frequency noise $\leq 2 \text{ Hz}^2/\text{Hz}$. The noise peaks at ca. 250 kHz are attributed to the laser's relaxation oscillation frequency. Red shows a commercial diode laser (NewFocus Velocity) for comparison, exhibiting at least 20 dB times more phase noise at similar frequencies. The noise measurement for the TiSa laser clearly indicates absence of the $\sin^2(\Omega\tau_0)$ pattern, visible in the measurement for the diode laser and expected for the classical laser noise interference, showing that the phase noise of the TiSa lasers was not observed. (B) Amplitude noise of the Ti:Sa characterised as relative intensity noise integrated over a 3 MHz bandwidth around the mechanical frequency for the used Ti:Sa laser. The solid line shows fit with $1/P$ dependence, characteristic of shot noise limited behavior.

Figure 10B). This means that, $C_{qq} < 5 \times 10^{-3}$, implying a negligible contribution to excess classical correlations and a negligible fraction of classical back-action motion, $n_{\text{CBA},q} < 0.005 \cdot n_{\text{QBA}}$, compared to quantum back-action.

Laser phase noise was upper-bounded using a self-heterodyne measurement [37] with a 400 m fiber delay line. The self-heterodyne signal can be described by the formula (after shifting the beat-note to zero frequency)

$$\bar{S}_{II}[\Omega] \propto \frac{\pi}{2} \delta[\Omega] + \sin^2\left(\frac{\Omega\tau_0}{2}\right) \bar{S}_{\phi\phi}[\Omega], \quad (\text{B7})$$

where τ_0 is the delay and $\bar{S}_{\phi\phi}[\Omega]$ is the laser phase noise spectral density. The measured signal for the laser is shown in fig. 10A, where the vertical scale is calibrated using the known mean photon flux in the beat note carrier. For the Ti:Sa laser (the blue curve in Figure 10A) the absence of the characteristic $\sin^2(\Omega\tau_0)$ interference pattern suggests that laser phase noise is below the sensitivity of the measurement. Although the laser is expected to be quantum-noise-limited at frequencies well above the relaxation oscillation frequency ($\approx 400 \text{ kHz}$), our measurements can only provide a conservative upper-bound for the frequency noise to be at the level of $2 \text{ Hz}^2/\text{Hz}$ (in comparison, frequency noise of a commercial external cavity diode laser, also shown in Figure 10A, is 20 dB larger). This upper bound on the excess phase noise, together with large optical linewidth (κ) strongly suppresses the influence of C_{pp} and leads to an estimated back-action motion that is below a factor 0.0025 compared to the quantum mechanical contribution. Intrinsic cavity frequency noise, for example from thermoelastic [38] or thermorefractive [39] processes, can also lead to a finite value of C_{pp} . In the current experiments, broadband measurements of cavity transmission on phase quadrature, shown in fig. 11, suggests a conservative upper bound of $C_{pp} < 10$ at frequencies around Ω_m . Using a length-balanced homodyne interferometer for detection, classical phase noise in the measurement imprecision could also be bounded by 0.1%.

6. Excess detection noise due to taper vibrations

While the amplitude quadrature of the employed Ti:Sa laser is quantum-noise-limited at Fourier frequencies around the mechanical oscillator resonance, analysis of the displacement spectra reveals that there is an additional background present in the measurement, that reaches 25% of the shot noise level around the mechanical oscillator Fourier frequencies for the largest powers used in the experiment ($50 \mu\text{W}$). This structured background, extrinsic to the laser, is revealed around the amplitude quadrature where sensitivity to broadband thermomechanical noise is significantly reduced, as shown in fig. 11. By analysing the spectral dependence of the noise, we find evidence in support of the hypothesis that it is due to thermal motion of the stressed tapered fiber softly clamped on two supports. The inset of fig. 11 plots the free spectral range of the noise peaks as a function of frequency, indicated with orange data points, which is seen to follow a power law $\propto \Omega^{0.31}$. Such a power law scaling is consistent with phase velocity dispersion of the lateral vibrations of an elastic cylinder [40, 41]. As a second check of the hypothesis that

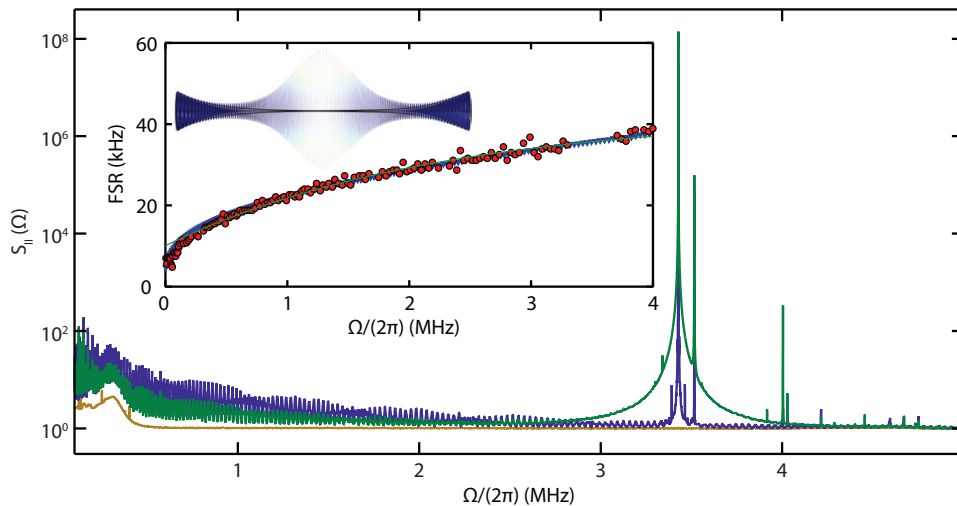


FIG. 11. Broadband homodyne spectrum of cavity transmission at phase (green) and amplitude (blue) quadratures, for a power of $P = 24 \mu\text{W}$. Local oscillator shot noise is shown in yellow. Inset shows measured free-spectral range of noise peaks as function of frequency (orange), with power law fit, $\propto \Omega^{0.31}$. Finite element model calculation of the free-spectral range is shown in blue. Image shows a fiber harmonic near 3.5 MHz.

the excess noise originates from fiber vibrations, the eigenmodes of a realistic tapered fiber geometry are computed using finite element modeling. The model incorporates the known geometry of the taper, which is ca. 25 mm long and $80 \mu\text{m}$ in diameter at the clamping points. The taper profile is modeled as exponential in cross-section, as expected for a taper pulled with a uniform heat source [42]. The model assumes the center of the taper is $1 \mu\text{m}$ in diameter. The prediction of this mode, shown as blue data point in Figure 11 inset, closely matches the measured data (orange).

Also, in contrast to guided-acoustic wave Brillouin scattering [43], the vibrational noise peaks are only present when the taper is coupled to the microcavity. We suspect that reactive and dispersive coupling of the tapered fiber to the cavity leads to transduction of its motion onto both transmitted amplitude and phase quadratures.

Appendix C: Quantum-enhanced force sensitivity

Consider estimation of an arbitrary force, δF , acting on the mechanical oscillator. The homodyne photocurrent spectrum carries information about the force eq. (A8), viz.

$$\bar{S}_{II}^{\theta, \text{hom}}[\Omega] = 1 + \frac{4\eta C \Gamma_m}{x_{zp}^2} \left[|\chi[\Omega]|^2 \left(\bar{S}_{FF}[\Omega] + \bar{S}_{FF}^{\text{QBA}}[\Omega] \right) \sin^2 \theta + \frac{\hbar}{2} \sin(2\theta) \text{Re} \chi[\Omega] \right]. \quad (\text{C1})$$

The spectrum of the applied force $\bar{S}_{FF}[\Omega]$ can be estimated from the photocurrent spectrum via,

$$\begin{aligned} \bar{S}_{FF}^{\text{est}, \theta}[\Omega] &:= \frac{\bar{S}_{II}^{\theta, \text{hom}}[\Omega]}{(4\eta C \Gamma_m / x_{zp}^2) |\chi[\Omega]|^2 \sin^2 \theta} \\ &= \bar{S}_{FF}[\Omega] + \bar{S}_{FF}^{\text{QBA}}[\Omega] + \underbrace{\frac{x_{zp}^2}{4\eta C \Gamma_m |\chi|^2 \sin^2 \theta}}_{\bar{S}_{FF}^{\text{imp}, \theta}} + \hbar \cot \theta \frac{\text{Re} \chi}{|\chi|^2}. \end{aligned} \quad (\text{C2})$$

Here, the first term represent the spectral density to be estimated. The second term, positive at all frequencies, is the contamination in the measurement record due to quantum back-action. The third, also positive term, is the imprecision due to shot-noise in the detection. The last term is due to quantum correlations between the back-action and imprecision in homodyne measurement record that can be negative at some frequencies, providing for reduced uncertainty in the ability to estimate the force.

Note that precisely on resonance ($\Omega = \Omega_m$), and/or, for phase quadrature homodyne measurement ($\theta = \pi/2$), correlations do not contribute to the estimator; so any reduction in uncertainty can only be expected away from resonance for quadrature-detuned homodyne measurement.

For a fixed probe strength, i.e. fixed cooperativity C , there exists a frequency dependent homodyne phase at which the correlation and the imprecision $\bar{S}_{FF}^{\text{imp},\theta}$ achieve an optimal trade-off. This optimal angle $\theta_{\text{opt}}[\Omega]$ is determined by,

$$\cot \theta_{\text{opt}}[\Omega] = -\frac{\hbar}{x_{\text{zp}}^2} 2\eta C \Gamma_m \text{Re } \chi[\Omega] = 4\eta C \frac{\Omega_m \Gamma_m (\Omega^2 - \Omega_m^2)}{(\Omega^2 - \Omega_m^2)^2 + (\Omega \Gamma_m)^2}. \quad (\text{C3})$$

At this optimal angle, the spectrum of the force estimator takes the form,

$$\bar{S}_{FF}^{\text{est},\theta_{\text{opt}}}[\Omega] = \bar{S}_{FF}[\Omega] + \bar{S}_{FF}^{\text{QBA}}[\Omega] + \frac{x_{\text{zp}}^2}{4\eta C \Gamma_m |\chi[\Omega]|^2} - \eta C \Gamma_m \frac{\hbar^2}{x_{\text{zp}}^2} \left(\frac{\text{Re } \chi[\Omega]}{|\chi[\Omega]|} \right)^2. \quad (\text{C4})$$

Noting that the third term is simply $\bar{S}_{FF}^{\text{imp},\pi/2}$, and that $\bar{S}_{FF}^{\text{QBA}}[\Omega] = C \Gamma_m \frac{\hbar^2}{x_{\text{zp}}^2}$, this equation can be re-expressed in the suggestive form,

$$\bar{S}_{FF}^{\text{est},\theta_{\text{opt}}}[\Omega] = \bar{S}_{FF}[\Omega] + \bar{S}_{FF}^{\text{imp},\pi/2}[\Omega] + \bar{S}_{FF}^{\text{QBA}}[\Omega] \left[1 - \eta \left(\frac{\text{Re } \chi_x[\Omega]}{|\chi_x[\Omega]|} \right)^2 \right]. \quad (\text{C5})$$

Thus, at the optimal detection angle, quantum correlations conspire to cancel quantum back-action (in the measurement record) and reduce the error in the force estimation compared to the conventional choice $\theta = \pi/2$, for which correlations are absent and

$$\bar{S}_{FF}^{\text{est},\pi/2}[\Omega] = \bar{S}_{FF} + \bar{S}_{FF}^{\text{imp},\pi/2}[\Omega] + \bar{S}_{FF}^{\text{QBA}}[\Omega]. \quad (\text{C6})$$

1. Correlation enhanced thermal force sensing

In the case of an oscillator in thermal equilibrium quantum correlations can yield improved sensitivity in the detection of the thermal force. In such a case the signal is the thermal force noise, i.e. $\bar{S}_{FF} = \bar{S}_{FF}^{\text{th}}$. Assuming that the recorded periodogram of the photocurrent has converged to the theoretical power spectrum, the homodyne angle dependent uncertainty in the spectral estimation of the thermal force may be defined by,

$$\epsilon_{\theta}[\Omega] := \bar{S}_{FF}^{\text{est},\theta}[\Omega] - \bar{S}_{FF}^{\text{th}}[\Omega]. \quad (\text{C7})$$

The enhancement in sensitivity attained for measurement at the optimal quadrature θ_{opt} , compared to the conventional measurement on phase quadrature, is quantified by,

$$\xi_{\text{th}}[\Omega] = \frac{\epsilon_{\pi/2}[\Omega]}{\epsilon_{\theta_{\text{opt}}}[\Omega]} = \frac{\bar{S}_{FF}^{\text{imp},\pi/2}[\Omega] + \bar{S}_{FF}^{\text{QBA}}[\Omega]}{\bar{S}_{FF}^{\text{imp},\pi/2}[\Omega] + \bar{S}_{FF}^{\text{QBA}}[\Omega] \left[1 - \eta \left(\frac{\text{Re } \chi[\Omega]}{|\chi[\Omega]|} \right)^2 \right]} \approx \left[1 - \eta \left(\frac{\text{Re } \chi[\Omega]}{|\chi[\Omega]|} \right)^2 \right]^{-1}, \quad (\text{C8})$$

where the last approximation is valid when $\bar{S}_{FF}^{\text{QBA}}[\Omega] \gg \bar{S}_{FF}^{\text{imp},\pi/2}[\Omega]$, i.e. in the limit of large cooperativity $C \gg 1$ and for frequency offsets around the mechanical resonance $|\Omega - \Omega_m|/\Gamma_m \ll 2\sqrt{\eta}C$. In this regime $\xi[\Omega] > 1$ and quantum-enhanced force sensitivity can be realized, with the enhancement factor being limited by the finite detection efficiency η and the imaginary part of the mechanical susceptibility. The back-estimated factors $\xi_{\text{th}}[\Omega]$ for the parameters of our experiment are shown in fig. 12 and demonstrate thermal force sensitivity enhancement up to 25%.

The ability to better estimate the thermal force over a broad range of frequencies may open up opportunities for probing the structure of the weak thermal environment that the oscillator is coupled to.

2. Correlation enhanced external force sensing

If an optomechanical system is used for external incoherent force detection, the thermal force itself becomes a part of the noise background. We now consider the sensitivity enhancement in such a case, i.e. $\bar{S}_{FF} = \bar{S}_{FF}^{\text{ext}} + \bar{S}_{FF}^{\text{th}}$, and the error is,

$$\epsilon_{\theta}[\Omega] := \bar{S}_{FF}^{\text{est}}[\Omega] - \bar{S}_{FF}^{\text{ext}}[\Omega]. \quad (\text{C9})$$

The corresponding expression for the sensitivity enhancement,

$$\xi_{\text{ext}}[\Omega] = \frac{\epsilon_{\pi/2}[\Omega]}{\epsilon_{\theta_{\text{opt}}}[\Omega]} = \frac{\bar{S}_{FF}^{\text{imp},\pi/2}[\Omega] + \bar{S}_{FF}^{\text{th}}[\Omega] + \bar{S}_{FF}^{\text{QBA}}[\Omega]}{\bar{S}_{FF}^{\text{imp},\pi/2}[\Omega] + \bar{S}_{FF}^{\text{th}}[\Omega] + \bar{S}_{FF}^{\text{QBA}}[\Omega] \left[1 - \eta \left(\frac{\text{Re } \chi[\Omega]}{|\chi[\Omega]|} \right)^2 \right]}, \quad (\text{C10})$$

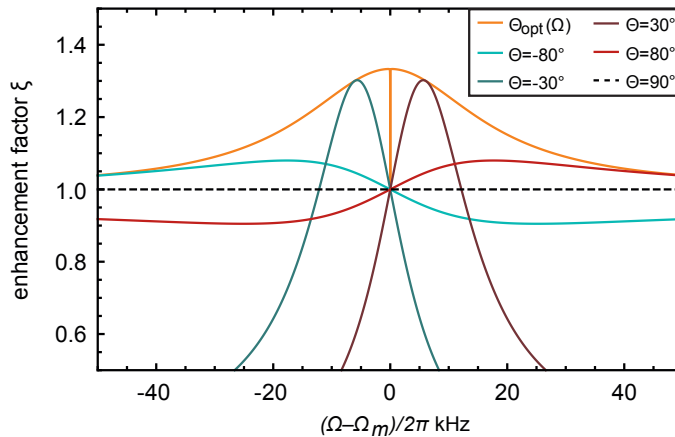


FIG. 12. Quantum-enhanced sensitivity to thermal force for the parameters realized in the current experiment, assuming input power = $25 \mu\text{W}$. Plot shows the enhancement factor $\xi_\theta[\Omega]$, defined in eq. (C8), as a function of Fourier frequency and homodyne angle θ . The dashed black line corresponds to $\xi_{\pi/2}[\Omega]$, where force is estimated by phase quadrature detection, where backaction-imprecision correlations are absent. As the homodyne angle is detuned from phase quadrature, enhancement of up to 25% can be observed, limited by the detection efficiency of similar magnitude. The yellow curve shows the theoretically ideal detection scheme, where the homodyne angle is frequency dependent (eq. (C3)), so that broadband enhancement is realized.

indicates an additional constraint to be met due to the presence of the thermal force – the quantum backaction force needs to be comparable to the thermal force. For the room temperature experiments to date the limit $n_{\text{QBA}}/n_{\text{th}} \ll 1$ (with $n_{\text{th}} \gg 1$) have been relevant, so, again for the case $\bar{S}_{FF}^{\text{QBA}} \gg \bar{S}_{FF}^{\text{imp}, \pi/2}$,

$$\xi_{\text{ext}}[\Omega] \approx 1 + \eta \frac{n_{\text{QBA}}}{n_{\text{th}}} \left(\frac{\text{Re} \chi[\Omega]}{|\chi[\Omega]|} \right)^2, \quad (\text{C11})$$

and quantum-enhanced sensitivity to external force can be realized far off resonance, if QBA is significant compared to thermal noise.